

Architectural performance assessment of an electric vertical take-off and landing (e-VTOL) aircraft based on a ducted vectored thrust concept

Author: Dr. P. Nathen^a,
Reviewer 1: Prof. Dr. A. Bardenhagen^b,
Reviewer 2: Prof. Dr. A. Strohmayer^c,
Reviewer 3: Prof. R. Miller^d,
Reviewer 4: Dr. S. Grimshaw^d,
Reviewer 5: Dr. J. Taylor^d

^a*Lilium GmbH, Claude-Dornier Straße 1, 82234 Wessling, Germany*

^b*Technische Universität Berlin, Institut für Luft- und Raumfahrt, Marchstraße 12, D-10587 Berlin, Germany*

^c*Universität Stuttgart, Institut für Flugzeugbau, Pfaffenwaldring 31, 70569 Stuttgart, Germany*

^d*Whittle Laboratory, University of Cambridge, 1 JJ Thomson Avenue, Cambridge, UK*

Acknowledgment

I would like to thank Prof. Dr. Bardenhagen, Prof. Dr. Strohmayer, Prof. Miller, Dr. Grimshaw and Dr. Taylor for the diligent proof read, the technical assessment of the proposed e-VTOL aircraft on an aircraft architecture level and the valuable comments on the technical consistency of the content in the following work. No public or private funds were involved in this collaboration.

Abstract

Urban and Regional Air Mobility (UAM & RAM) seek to extend passenger transportation to the third dimension and a variety of electric vertical take-off and landing (e-VTOL) aircraft concepts have been proposed to unlock this new mode of transport. The UAM market requires an operating range of 5–40km at a speed of 70–120km/h, and the RAM market, involving connection between metropolitan areas, requires an operating range of 100–300km, and a speed of beyond 200km/h.

The RAM market offers significant commercial and economic opportunities as it creates a customer proposition of greatly reduced travel time and improved network effectiveness. Because the aircraft must take-off and land from city centres it is important that they have low noise emissions. It is also important that the aircraft can carry a sufficient payload over the required range to make the business model economic.

This paper analyses the performance and range of a Ducted Vectored Thrust

Concept (DVTC) e-VTOL, which is specifically optimised to meet the low-noise vertical take-off, long range and high payload requirements of the RAM market. The specific aircraft analysed is the Lilium jet. The aircraft is 7-seater with a cruise speed of $300km/h$ and maximum take-off mass of $3,175kg$. The paper shows that assuming a battery energy density of $320Wh/kg$, the maximum range of the aircraft is $261km$. At the same time, the ducted fan architecture allows the noise emissions in take-off and landing hover to be below $60dB(A)$ at a distance of $100m$ distance. This performance makes the aircraft ideal for operation in the RAM market.

1. Architectural design space for e-VTOL aircraft

The design of e-VTOL aircraft for passenger transport is a new field, see Thippavong et al. (2018) and Whittle (2018). Five degrees-of-freedom (DOF) drive the design: payload, speed, range, noise and simplicity. These degrees-of-freedom are strongly interlinked and the improvement of one parameter often disadvantages one or more of the others. Additional degrees-of-freedom, which are not considered in this paper, include safety and costs. They are essential for inner city operations and to enable scaling of mobility services. For simplicity, however, this paper only considers the impact of the first five degrees-of-freedom on the aerodynamic performance of the Lilium jet. In Figure 1,




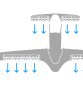
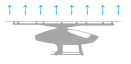



	Multicopter	Lift + Cruise	Tilt Rotor	Ducted Vectored Thrust
Aircraft				
				
UAM	✓	✓	✓	✓
RAM	✗	⊖	✓	✓

Figure 1: Comparison of different e-VTOL concepts. All data is based on estimates from company data in the public domain.

the four most common types of e-VTOL aircraft architectures are shown and compared against their predicted application in UAM and RAM markets. The choice of architecture determines the trade between the different DOFs and ultimately determines the cruise and hover efficiency and the noise emissions of an aircraft. As e-VTOL aircraft are designed to operate close to and within city centers, special emphasis should be given to safety and noise during the conceptual design phase. The conceptual design of an e-VTOL aircraft results from the combination of different DOFs and determines the technological complexity while varying a single DOF. Discussion of these trade-offs are provided by Bacchini and Cestino (2019); Polaczyk (2019); Clarke et al. (2019).

The first category of e-VTOL is the multicopter architecture. This configuration is relatively simple and can be very efficient during vertical take-off, landing, and hovering, due to low disc-loading. However, without wings, multicopters

lack cruise efficiency, which limits their application to UAM markets only. A more detailed review of multicopter architecture can be found in Pradeep and Wei (2019).

The second category of e-VTOL is the lift & cruise architecture. These merge the multicopter, for vertical take-off and landing, with a standard aircraft for cruise flight. Doing so allows the aircraft to achieve both efficient vertical take-off and landing, and efficient cruise. In order to maximize range for these concepts, the propellers needed for VTOL are designed with fewer blades and shorter chords, in order to reduce drag during cruise flight. The small size of the propellers for VTOL operation create a significant challenge in terms of noise emissions, due to increased blade tip speeds.

The third category of e-VTOL is the tilt rotor architecture which either involves the wing and propellers, or the propellers alone, tilting. This allows the propeller axis to rotate through 90 degrees as the aircraft transitions from hover to forward flight. In general, this architecture allows a propeller to be designed which is more optimal than would be possible with a lift & cruise architecture of aircraft. However, this comes at the price of higher technical complexity and larger overall size and weight, due to the tilt and variable pitch mechanisms. The hover requirement requires the propellers to be large, with low tip speed and low disc loading. This means that either the motors need to be large and heavy, to produce the low speed torque, or a gearbox is required, eventually interfering with the structure. Further challenges can occur in the design of the flight dynamics during the flight transition process, although significant progress has been reported in Chauhan and Martins (2020). A design space evaluation of tilt rotors is given in Hendricks et al. (2019).

The three categories of e-VTOL discussed above all rely on a propulsion system based on propellers. The fourth category of e-VTOL are known as ducted fan architectures. A major advantage of ducted fans over unducted propellers is that the duct acts to significantly mitigate noise, both blade passing and broadband. This is achieved both by the presence of the duct and by acoustic liners mounted within them. This is of particular importance when the payload of aircraft is increased. If the design requirement is to operate from existing helipads then the maximum footprint of the aircraft is limited, i.e. the largest dimension must be less than 14m. When the payload is raised on a propeller aircraft the only way of holding the level of noise constant is to hold the disc loading constant and to therefore increase the size of the propellers. When the payload is raised on a ducted fan the designer has an extra degree of freedom: they can let the disc loading rise and use the duct and acoustic treatment to limit the increase in noise. For a fixed size of footprint this results in a ducted fan aircraft having a payload which is approximately 40% higher than a propeller aircraft.

Ducted fans have efficiency advantages which arise from the presence of the duct. Blade tip losses are reduced and the presence of a stator row removes exit

swirl. Another advantage of ducted fans is that the duct can contain a blade-off in the case of blade loss or bird strike making them safer than open propellers. The main disadvantage of ducted fans is that because of the higher disc loading, as discussed above, the hover power is higher than for propeller aircraft.

When employing ducted fans, two aircraft types are feasible. In the first type the ducted fan is located away from the airframe so that aerodynamic interactions are minimised; this type of aircraft is similar to conventional large civil airliners. The second type integrates the ducted fan closely with the fuselage and wings meaning there is close aerodynamic coupling. This architecture is similar to that used in future aircraft concepts where boundary layer ingestion is applied, see Hall and Crichton (2006).

The Lilium jet, Lilium (2019b), is an example of the second type of ducted fan concept, where the ducted fan and wing are closely coupled. 36 ducted fans are integrated into the aircraft's canard and main wings. We refer to this as the Ducted Vectored Thrust Concept (DVTC) with distributed electric propulsion (DEP).

In the Lilium jet the ducted fans are compactly embedded close to the trailing edge of the wing. This has three main advantages: first, the ducted fan helps to keep the flow over the wing attached, enabling controlled flow over the wings throughout the aircraft's flight envelope, which provides improved flight performance. Second, it allows the ducted fans to be used for thrust vectoring, making aerodynamic control surfaces such as rudders, ailerons or tails obsolete resulting in weight savings and complexity reduction. Third, the compact packaging allows for improved cruise flight performance. By integrating the smaller ducted fans in the form of DEP at the trailing edge of the wing, around a 30% reduction in aircraft wetted duct surface area is achieved, thus reducing drag and increasing range. Finally, it is worth noting that the higher rotational speed of the fans, relative to propellers, means that they are less likely to excite low frequency structural modes in the airframe providing improved safety and user experience.

The ducted fan architecture of the Lilium jet has a disc loading which is up to 10 times higher than some open propeller architectures making it less efficient in hover. This results in a higher power consumption during the hover phase when compared to open propellers. However, the paper will show that the proposed DVTC aircraft architecture only spends a small fraction of the flight mission in hover flight, and so the contribution of the increased hover power has a relatively small effect on the overall energy of the flight mission. Lilium has therefore concluded that the economic benefit of a heavier aircraft with higher payload and lower noise emission outweighs the higher hover flight power consumption.

The aim of this paper is to demonstrate the mission capability of a DVTC e-

VTOL aircraft which can address the market needs of UAM and RAM without facing the same noise challenges as propeller concepts. This paper is structured as follows: Section 2 details the aircraft requirements and specification. Section 3 describes the approach to the analysis. Section 4, analyses the aircraft performance. Section 5, provides an overview of the battery, powertrain and electric motor technologies, and Section 6, analyses the sensitivity to key input parameters.

2. Design of a DVTC e-VTOL aircraft

The aircraft is designed to meet the business requirements of the RAM markets where the minimum mission range $R_{min} = 200km$ at a nominal operating speed of $v_{cr} = 300km/h$ is required. The high speed offers significant reduction in inter-city flight times. The maximum take-off mass (MTOM) of $MTOM = 3,175kg$ complies with current SC-VTOL regulation, see EASA (2019).

To ensure a profitable and scalable business case, it is assumed that the aircraft can transport 6 passengers with luggage with a total mass of $m_{pax} = 6 \cdot 100kg$. The pilot’s mass is assumed to be $m_p = 100kg$. This leads to a total payload mass of $m_{pl} = 700kg$. The ratio of payload mass to maximum take-off mass is therefore $\mu_{pl} = \frac{m_{pl}}{MTOM} = 0.22$ and the ratio of empty mass to maximum take-off mass is $\mu_s = \frac{m_s}{MTOM} = 0.48$. These values are typical of the range reported in the literature, see Kim et al. (2018). Thus, the ratio of battery mass to maximum take-off mass is $\mu_b = \frac{m_b}{MTOM} = 0.30$, again typical of the range seen in the literature for e-VTOL aircraft, see Bacchini and Cestino (2019) and Polaczyk (2019).

This results in a battery mass $m_b = 953kg$. Assumptions around battery technology are important and will be separately addressed in Section 5.1. We start by assuming an energy density of $e_b = 320Wh/kg$ which Lilium expects to be deployed in the first vehicle. The total stored energy is therefore

$$E_s = \mu_b \cdot MTOM \cdot e_b = 305kWh. \quad (1)$$

For all of our assessments we take the cell based energy density as an input parameter, as Lilium assumes the structural modules of the battery cells will be part of the empty aircraft structure.

The dimensions of the Lilium jet are shown in Figure 2. To make use of existing helipads and Final Approach and Take-Off areas (FATOs), the span of the aircraft is $s_w = 13.9m$, the length, width, and height of the cabin are l_b , w_c , and h_c and the chord of the main wing is l_c .

The propulsion system is made up of electrically driven ducted fans embedded in the wings. The size, power and speed of the fans is chosen through a

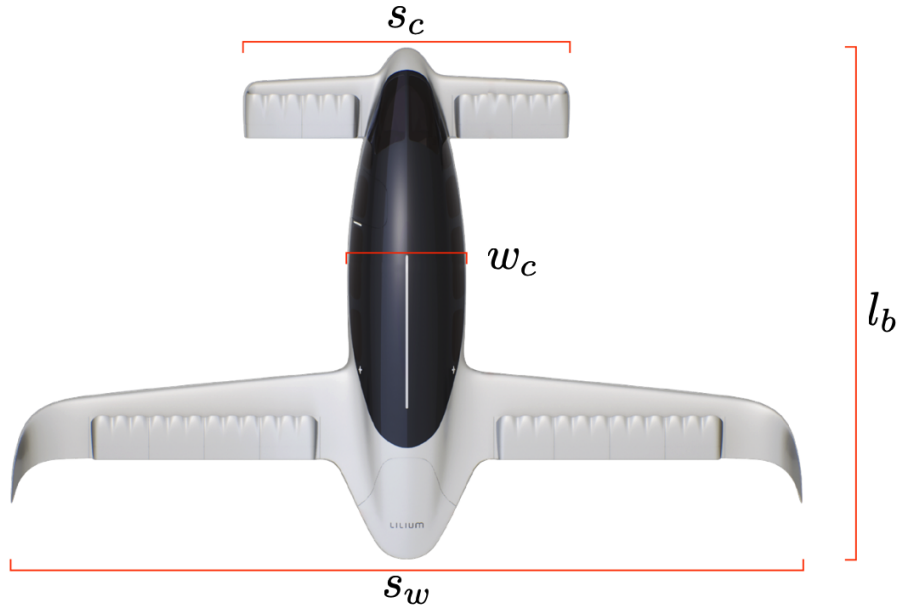


Figure 2: The Lilium jet architecture. Picture taken from Lilium (2019a).

trade-off between noise, cruise power consumption, hover power consumption, redundancy, DEP packaging efficiency, and engineering complexity. In the reference architecture the number of ducted fans is $n = 36$, and the diameter of the fan shroud is $d_s = 0.295m$. The fan's hub diameter $d_h = 0.12m$ is selected by the requirement to support the motor. The duct area, thus, is $A_d = 0.057m^2$. The ducted fans are split between the main wing and canard where $n_c/n_w = 0.5$, where n_c and n_w are the number of ducted fans on the canard and wing respectively. The length of the duct, in which the fan is located, is $l_s = 0.7m$. This results in a duct length to fan diameter ratio of ≈ 2.4 . A summary of the aircraft specification is given in Table 1.

Service and mass				Structure					Engines						
MTOM	μ_b	μ_s	μ_{pl}	s_w	s_c	l_b	w_c	h_c	n	A_d	$A_{j,h}$	$A_{j,cr}$	l_s	l_{stage}	l_{hub}
3,175kg	0.30	0.48	0.22	13.9m	6.3m	8m	1.7m	1.5m	36	0.057m ²	0.0742m ²	0.0513m ²	0.7m	0.4m	0.5m

Table 1: Initial sizing parameters for a DVTC based e-VTOL aircraft.

3. Performance analysis method

The aim of the analysis is to calculate the aircraft's range while retaining enough simplicity to allow the reader to gain a physical understanding of the key trades. The methodology introduced here, is applicable to any DVTC e-VTOL concept, captures the most important physics and gives a realistic estimate of

range. To begin the assessment, a flight mission is defined, shown in Figure 3. The mission can be divided into seven phases. The seven phases are made up of the four modes of flight listed below.

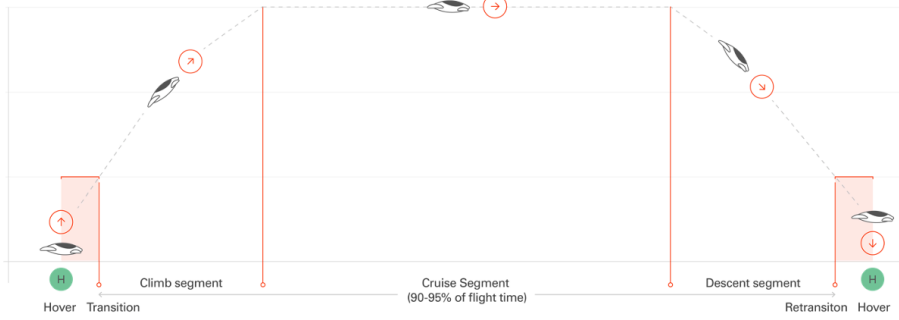


Figure 3: Flight phases for an e-VTOL mission for simplified calculations

- **Hover:** This is the period of the flight where the aircraft takes off and lands vertically. During hover the power demand of the battery P_h is constant.
- **Transition and re-transition:** This is the period of the flight where the aircraft is transitioning from hover into forward flight, and forward flight into hover. During transition, the power demand of the battery P_{tr} drops quadratically with time as the source of the aircraft lift changes from lift generated by the propulsors to lift from the wings.
- **Climb and descent:** This is the period of flight where the aircraft climbs to cruise altitude and accelerates to cruise speed. The climb power demand P_{cl} during this phase is assumed to be constant.
- **Cruise:** This is the period of flight where the aircraft is at constant altitude and speed. During cruise the power demand of the battery P_{cr} is constant. A nominal cruise altitude of $3000m$ will be used in this study. This is the altitude up to which a DVTC e-VTOL aircraft can operate without the need of a pressurized passenger cabin.

The methodology for calculating the power demand of the battery during the hover, transition, climb, and cruise periods of the flight are given in Section 3.1 -3.4 respectively. The methodology for calculating range is given in Section 3.5.

3.1. Hover power

The power extracted from the battery during hover P_h can be calculated using the overall efficiency $\eta_{0,h}$ of the propulsion system during hover

$$\eta_{0,h} = \frac{\text{power to jet}}{\text{battery power}} = \frac{0.5 \cdot \dot{m}_h \cdot v_{j,h}^2}{P_h}, \quad (2)$$

where $v_{j,h}$ is the jet velocity at nozzle exit during hover and \dot{m}_h is the total mass flow through the fans during hover. The overall hover efficiency can be written as

$$\eta_{0,h} = \frac{\text{power to jet}}{\text{power from battery}} = \underbrace{\frac{\text{power to electronics}}{\text{power from battery}}}_{\eta_{B,h}} \cdot \underbrace{\frac{\text{power to motors}}{\text{power from electronics}}}_{\eta_{PE,h}} \cdot \underbrace{\frac{\text{power to shaft}}{\text{power from motors}}}_{\eta_{M,h}} \cdot \underbrace{\frac{\text{power to flow}}{\text{power from shaft}}}_{\eta_{F,h}} \cdot \underbrace{\frac{\text{power to jet}}{\text{power from flow}}}_{\eta_{D,h}}, \quad (3)$$

where $\eta_{D,h}$ is the duct efficiency, $\eta_{F,h}$ the fan efficiency, $\eta_{M,h}$ the motor efficiency, $\eta_{PE,h}$ the power electronics efficiency and $\eta_{B,h}$ the battery efficiency.

The power use of the battery during hover can then be calculated by rearranging Equations (2) and (3) and by rewriting the equation for the kinetic energy flux of the jet in terms of the jet thrust (derivation given in Appendix A) to give

$$P_h = \frac{0.5 \cdot \dot{m}_h (v_{j,h})^2}{\eta_{0,h}} = \frac{\frac{1}{2} \frac{T_h^{3/2}}{\sqrt{\rho_h \cdot n \cdot A_{j,h}}}}{\eta_{F,h} \cdot \eta_{D,h} \cdot \eta_{PE,h} \cdot \eta_{M,h} \cdot \eta_{B,h}}, \quad (4)$$

see Spurk and Aksel (2019) or Trancossi and Madonia (2012). In Equation (4), T_h is the thrust of the propulsion system during hover, ρ_h is the air density during hover flight calculated for an international standard atmosphere, $A_{j,h}$ is the jet area of a single ducted fan in hover, and n is the number of ducted fans. During hover the thrust requirement is fixed by the weight of the aircraft.

It should be noted that the relationship between the kinetic energy flux of the jet and the thrust of the jet, shown in the numerator of (4) is only valid for the case of a ducted fan. For the case of a propeller with no outer duct the relationship between the kinetic energy flux and the thrust is

$$P_h^{open} = 0.5 \cdot \dot{m}_h \cdot v_{j,h}^2 = \frac{T_h^{3/2}}{\sqrt{2\rho_h n A_d}}, \quad (5)$$

see Bittner (2005). In Equation (5) A_d is the disc area of the open propeller.

3.2. Cruise power

The power extracted from the battery during cruise P_{cr} can be calculated using the efficiency of the propulsion system during cruise $\eta_{0,cr}$

$$\eta_{0,cr} = \frac{\text{power to aircraft}}{\text{battery power}} = \frac{D_{cr} \cdot v_{cr}}{P_{cr}}, \quad (6)$$

where D_{cr} is the drag of the aircraft, and v_{cr} is the cruise velocity of the aircraft. The efficiency in cruise can be written out as a product of efficiencies as

$$\eta_{0,cr} = \frac{\text{power to aircraft}}{\text{power from battery}} = \underbrace{\frac{\text{power to electronics}}{\text{power from battery}}}_{\eta_{B,cr}} \cdot \underbrace{\frac{\text{power to motors}}{\text{power from electronics}}}_{\eta_{PE,cr}} \cdot \underbrace{\frac{\text{power to shaft}}{\text{power from motors}}}_{\eta_{M,cr}} \cdot \underbrace{\frac{\text{power to flow}}{\text{power from shaft}}}_{\eta_{F,cr}} \cdot \underbrace{\frac{\text{power to jet}}{\text{power from flow}}}_{\eta_{D,cr}} \cdot \underbrace{\frac{\text{power to aircraft}}{\text{power from jet}}}_{\eta_{P,cr}}, \quad (7)$$

where $\eta_{P,cr}$ is the propulsive efficiency and the other efficiencies are the same as in Equation (3).

The power extracted from the battery during cruise can then be calculated by rearranging Equations (6) and (7) to give

$$P_{cr} = \frac{\sum_i D_{i,cr} \cdot v_{cr}}{\eta_{P,cr} \cdot \eta_{D,cr} \cdot \eta_{F,cr} \cdot \eta_{PE,cr} \cdot \eta_{M,cr} \cdot \eta_{B,cr}}, \quad (8)$$

where $\sum_i D_i$ indicates the summation of all individual drag components of the aircraft.

3.3. Transition and re-transition power

As discussed earlier the power extracted from the battery during transition drops quadratically with time as the source of the aircraft lift changes from lift generated by the ducted fans to lift from the wings. The power at the start of transition is equal to the hover power. By the end of the transition period the power has dropped by approximately a factor of $\kappa = 10$. For simplicity the power during transition is considered constant and equal to the average of power at the start of transition and the power at the end of transition.

$$P_{tr,avg} = (P_h + P_{tr,eff})/2, \quad (9)$$

where $P_{tr,eff} = P_h/\kappa$. Because in reality the power drops quadratically Equation (9) overestimates the power consumption and is therefore conservative. For simplicity the same power consumption relationship will be used for both transition and re-transition. During transition the aircraft accelerates at $0.2g$ from $0km/h$ to $v_{tr} = 150km/h$, resulting in each transition taking $t_{tr} = 21.2s$.

3.4. Climb and descent power

The relationship for the power extracted from the battery during climb P_{climb} is similar to the relationship for the power in cruise, Equation (8). The only difference is that the thrust of the aircraft must overcome both the air-

crafts drag and a component of its weight in the direction of flight. This can be written as

$$P_{cl} = \frac{(\sum_i D_{i,climb} + MTOM \cdot g \cdot \sin(\Phi)) \cdot v_{cl}}{\eta_{P,cl} \cdot \eta_{D,cl} \cdot \eta_{F,cl} \cdot \eta_{PE,cl} \cdot \eta_{M,cl} \cdot \eta_{B,cl}}. \quad (10)$$

During climb the altitude increases to $3000m$ and the speed increases from $150km/h$ to the cruise velocity $v_{cr} = 300km/h$. This means that climb power P_{cl} changes through the climb phase. In practice the component of the aircraft's weight term in the numerator of equation (10) is around 2 times larger than the drag term, depending on the constant climb angle Φ . This results in a higher climb power P_{cl} demand compared to cruise flight of approximately $P_{cl} \approx 2.25 \cdot P_{cr}$. For simplicity the climb power is assumed to be constant and calculated at a mean altitude of $1500m$ with a mean climb velocity $v_{cl} = 275km/h$.

During the descent the component of the aircraft weight, in the direction of flight, changes direction. This reduces the power requirement. In this analysis we will, for simplicity, set the engine power to 20% of the cruise power. This is a deliberately conservative choice and in practice the engine power will often be lower, set in practice by the particular architecture of the DVTC.

$$P_{des} = 0.2 \cdot P_{cr}. \quad (11)$$

It is common understanding, that the weight term in the numerator of equation (10) approximately cancels out during climb and descent and, thus, the approach taken here is a very conservative one during initial aircraft architecture assessment.

3.5. Aircraft range

The range of the aircraft can now be calculated using the relationships for the power during different phases of the flight. The total accessible energy in the battery is

$$E_{acc} = E_s \cdot (1 - SOC_{min}) \quad (12)$$

where E_s is the total stored energy and SOC_{min} is the minimum allowable state-of-charge. In this assessment we set $SOC_{min} = 10\%$.

The maximum energy use during a mission can be written in terms of power extracted from the battery during each phase of the flight.

$$E_s(1 - SOC_{min}) = \underbrace{t_h \cdot P_h}_{\text{Hover consumption}} + \underbrace{2 \cdot t_{tr} \cdot P_{tr}}_{\text{Transition consumption}} + \underbrace{t_{cl} \cdot (P_{cl} + P_{des})}_{\text{Climb consumption}} + \underbrace{P_{cr} t_{cr}}_{\text{Cruise consumption}}, \quad (13)$$

where t_h is the total time in hover, take-off and landing, t_{tr} is the total time in transition, take-off and landing, t_{cl} is the time in climb, and t_{cr} is the time in cruise. This can be rearranged to give an expression for the time in cruise, and multiplying by the cruise velocity v_{cr} gives a relationship for the cruise range of the aircraft. The distance travelled during the climb and descent phases of the flight are added to this to give the overall range:

$$R = \frac{v_{cr}}{P_{cr}} \cdot (E_s(1 - SOC_{min}) - t_h \cdot P_h - 2 \cdot t_{tr} \cdot P_{tr} - t_{cl} \cdot (P_{cl} + P_{des})) + 2 \cdot t_{cl} v_{cl}. \quad (14)$$

Equation (14) will be used for the range assessment of the aircraft.

4. Performance of the DVTC e-VTOL aircraft

In this section the analysis methodology developed in Section 3 will be applied to the nominal design of Lilium jet. The specification of the aircraft, which will be used in this analysis, is given in Section 2.

The analysis starts by calculating the aircraft’s cruise drag, the efficiencies of the propulsion system and the power use in each phase of flight. The values for the aircraft’s drag and efficiencies are summarised in Table 2. These values are then be used to calculate the aircraft’s range. Finally a noise assessment of the propulsion system will be undertaken.

Flight state	Drag	Propulsion			Motor and power electronics		Battery
	D	η_P	η_D	η_F	η_M	η_{PE}	η_B
Hover	–	–	0.96	0.88	0.92	0.95	0.80
Cruise	1705N	0.94	0.92	0.83	0.95	0.98	0.98
Climb	1698N	0.87	0.95	0.88	0.95	0.98	0.98

Table 2: Calculated efficiencies from Section 4 being used for the performance assessment.

4.1. Cruise drag

For the cruise phase of flight we assume the aircraft operates at an altitude of 3000m, flying at a cruise speed $v_{cr} = 300km/h$ where the air density is $\rho_{cr} = 0.91kg/m^3$ (see the "International Standard Atmosphere" (ISA)).

The total drag of the aircraft in cruise D_{cr} is the sum of the drags of each part of the aircraft, see Dole et al. (2016) and Kuchemann (2012):

$$D_{cr} = D_c + D_w + D_f + D_i, \quad (15)$$

where D_c is the cabin drag, D_w is the wing drag, D_f is the flap drag, and D_i is the induced drag.

4.1.1. Cabin drag

The ideal drag of the aircraft cabin, see Nicolosi et al. (2015) among others, can be calculated as

$$D_{c,ideal} = C_{D,c} \cdot 0.5 \cdot \rho_{cr} \cdot S_{c,\emptyset} \cdot v_{cr}^2 = 248N, \quad (16)$$

where the cabin drag coefficient is $C_{D,c} = 0.039$ and $S_{c,\emptyset}$ is the frontal area of the cabin. The frontal area of the cabin is

$$S_{c,\emptyset} = \frac{\pi}{4} \cdot \left(\frac{w_c + h_c}{2} \right)^2 = 2.01m^2, \quad (17)$$

where w_c is the cabin width, and h_c the cabin height.

Because the aircraft is of a canard design it is assumed that wing interference drag increases the cabin drag by 30%. The final cabin drag is

$$D_c = D_{c,ideal} \cdot 1.3 = 322N. \quad (18)$$

4.1.2. Wing drag

The drag of the wing D_w is given by

$$D_w = C_{D,w} \cdot 0.5 \cdot \rho_{cr} \cdot S_w \cdot v_{cr}^2, \quad (19)$$

where $C_{D,w}$ is the wing drag coefficient and S_w is the wing area. For a wing thickness to chord ratio of $t/l_c = 0.12$ and a fully turbulent boundary layer at a Reynolds number in the order of $\mathcal{O}(10^7)$, we find a reasonable value of $C_{D,w} = 0.014$, see Schlichting and Truckenbrodt (2001a,b).

The wing area S_w is given by

$$S_w = l_c \cdot (s_w - w_c) - n_w \cdot l_s \cdot d_s, \quad (20)$$

where in the first term on the right hand side represents the area of the whole wing, and the second term represents the area of the wing that has been removed and replaced with the ducted fans, see green wing surfaces in Figure 4. In Equation (20) l_c is the wing chord, s_w is the wing span, w_c is the cabin width, n_w is number of ducted fans on the wing. l_s is the length of the flap and d_s is the diameter of the fan shroud. Using the wing and fan dimensions from Section 2, Equation (20) gives a wing area of

$$S_w = 8.464m^2, \quad (21)$$

Substituting this into Equation (19) gives a wing drag of

$$D_w = 374N, \quad (22)$$

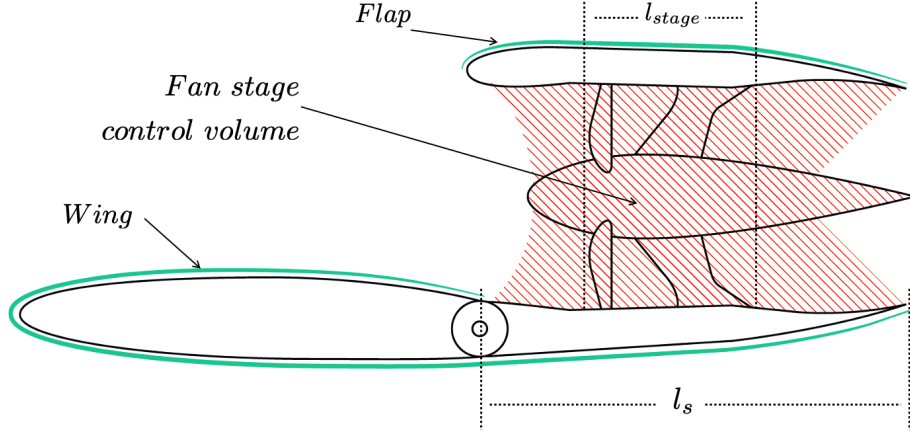


Figure 4: Wing and flap configuration. The scales, sizes, proportions, details and measurements are not implemented in the real aircraft and shall serve only for illustrative purposes. Green areas mark the surfaces being used to calculate wing drag D_w and flap drag D_f . The fan stage efficiency η_F is effective over the length l_{stage} . The duct efficiency η_D is effective over the remaining red length $l_s - l_{stage}$.

4.1.3. Flap drag

The flap is the nacelle of the ducted fan, shown in Figure 4. It is referred to as the flap because it is actuated and can pitch rearward. The drag of the flap is defined as the outer surface of the nacelle, shown in green in Figure 4. There are n_w ducted fans in the flap on the wing and n_c ducted fans on the canard, shown in Figure 2. The flap drag will be defined as the combined drag on the $n = n_w + n_c$ ducted fans on the wing and canard. The drag of the flap D_f is therefore given by

$$D_f = C_{D,f} \cdot 0.5 \cdot \rho_{cr} \cdot A_{flap,o} \cdot v_{cr}^2, \quad (23)$$

where $C_{D,f}$ the drag coefficient of the flaps, and $A_{flap,o}$ is the projected surface area of the flaps

$$A_{flap,o} = l_s \cdot d_s \cdot n = 7.434m^2. \quad (24)$$

The flap is a lifting surface and therefore we set $C_{D,f} = 0.017$. Substituting this into Equation (23) gives

$$D_f = 399N. \quad (25)$$

4.1.4. Induced drag

The induced drag D_i can be calculated, see Schlichting and Truckenbrodt (2001a,b), as

$$D_i = \frac{2 \cdot (MTOM \cdot g)^2}{\rho_{cr} \cdot \pi \cdot v_{cr}^2 \cdot s_w^2 \cdot e}, \quad (26)$$

where for a canard configuration the Oswald factor is $e = 0.83$, see Kroo (2001, 1982). Substitution of the Oswald factor into Equation (26) gives an induced drag of

$$D_i = 610N. \quad (27)$$

4.1.5. Total drag

The total drag in cruise is therefore

$$D_{cr} = D_c + D_w + D_f + D_i = 1,705N. \quad (28)$$

This allows a lift to drag ratio to be calculated for the aircraft. The lift is set by the weight of the aircraft $L = MTOM \cdot g$ giving

$$\Omega = L/D = \frac{MTOM \cdot g}{D} = 18.26. \quad (29)$$

The simple analysis employed in this paper does not account for the close aerodynamic coupling between the wing and ducted fan. To quantify the interaction between the wings and the ducted fan intake, for example, would require higher fidelity tools such as CFD. The boundary layer on the top of the wing is directly ingested into the ducted fan. This means that the low velocity air in the boundary layer does not have a chance to mix out downstream in the wing's wake, and instead is re-energized in the ducted fan. This effect will act to raise the overall cruise efficiency. At the same time the non-homogeneous flow entering the fan will act to lower fan efficiency. If correctly designed it is likely that this boundary layer ingestion mechanism can be exploited to reduce the power consumption of the aircraft in cruise. However, this is beyond the scope of this paper and in this analysis its beneficial effects will be ignored.

4.2. Efficiencies

Each of the efficiencies, described in Section 3, will be calculated in turn.

4.2.1. Fan efficiency

A major design challenge is designing a fan which will operate efficiently at both cruise and hover. The Lilium jet solves this problem using a variable area nozzle (VAN) at the exit of the duct, as shown in Figure 5. Changing the area of the exit nozzle moves the operating point of the fan, allowing it to be moved to a more efficient operating point. This solution is similar to that described by Hall and Crichton (2006) where variable area nozzles are used to optimize take-off and cruise performance in a future civil aircraft concept. The area of

the jet is defined by σ , the ratio of the diameter of the exit nozzle A_j and the area of the duct in which the fan is located A_d

$$A_j = \sigma A_d. \quad (30)$$

For hover we set $\sigma_h = 1.3$ and for cruise $\sigma_{cr} = 0.9$ resulting in $A_{j,h} = 0.0742m^2$ and $A_{j,cr} = 0.0513m^2$. At hover the blade tip Mach number is $Ma_{b,tip,h} = 0.45$ and the chord based Reynolds number of the rotor is $Re_{r,h} \approx 610 \cdot 10^3$. At cruise the blade tip Mach number is $Ma_{b,tip,cr} = 0.26$ and the chord based Reynolds number of the rotor is $Re_{r,cr} \approx 280 \cdot 10^3$. See Appendix B for the detailed calculation procedure.

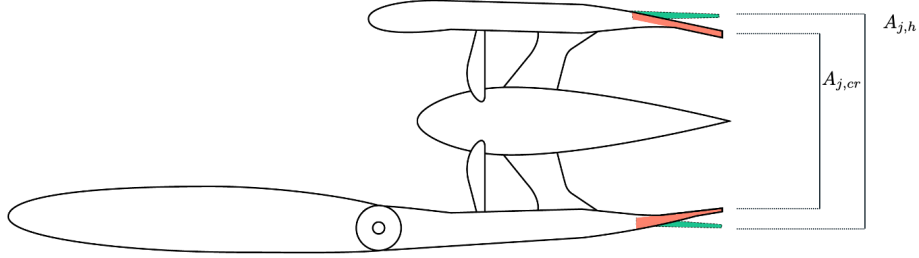


Figure 5: Illustrative representation of the variable nozzle concept. $A_{j,h}$ and $A_{j,cr}$ represent the effective jet area in hover and cruise flight respectively.

The effect of changing the area of the variable area nozzle on the fan operating point is shown in Figure 6, where the fan stage loading coefficient ψ and flow coefficient ϕ are defined as

$$\psi = \frac{\Delta h_0}{u_{b,mean}^2}; \quad \phi = \frac{v_{in}}{u_{b,mean}}. \quad (31)$$

Δh_0 is the stagnation enthalpy across the fan, $u_{b,mean}$ is the blade velocity at mass averaged radius r_{mean} (see Appendix B), and v_{in} is the axial velocity at fan inlet. The shape of the characteristic and the particular values of the flow and stage loading coefficients are calculated in Appendix B. Figure 6 shows an illustrative example of how stage loading and fan efficiency vary with flow coefficient. The black dot represents the hover operating point and the two white points represent the cruise operating point with the variable exit nozzle set at two different areas. For the concept described in this paper, the fan is designed to have peak performance during hover flight with an estimated isentropic efficiency $\eta_{F,h} = 0.88$ at $\sigma_h = 1.3$. This leads to a flow and stage loading coefficient of $\phi_h = 1.09$ and $\psi_h = 0.40$ for hover flight. At cruise flight conditions, the same fan, with the same variable exit nozzle setting, $\sigma = 1.3$ would have flow and stage loading coefficients of $\phi = 1.47$ and $\psi = 0.10$. At this high flow coefficient, a fan could drop in isentropic efficiency by $\Delta\eta_{aero} \approx -20\%$.

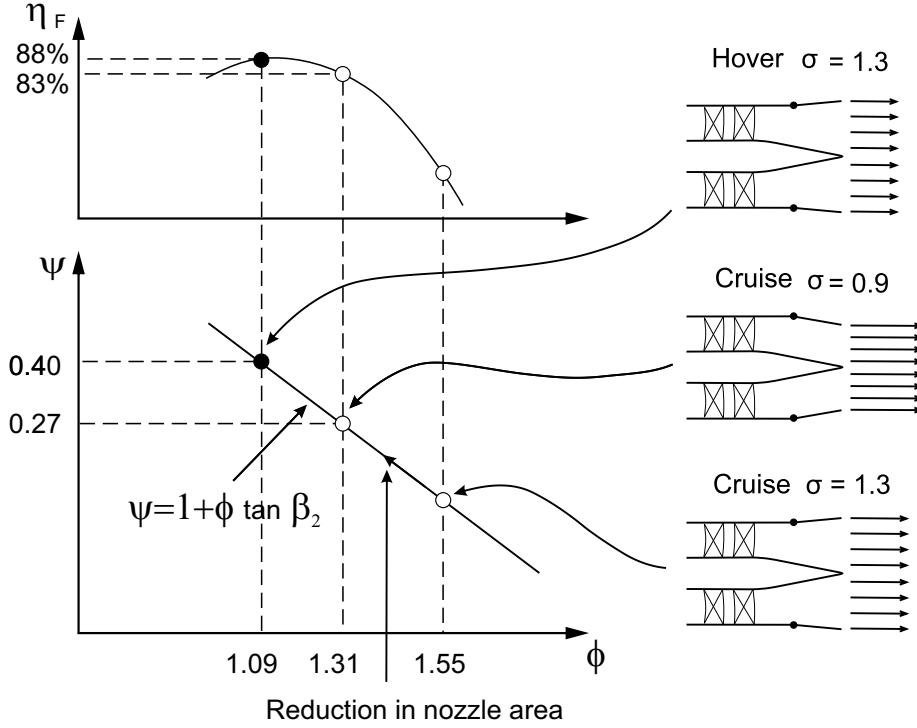


Figure 6: Effect of a variable area nozzle on fan performance.

At the cruise operating point, closing the exit nozzle area to $\sigma = 0.67$ would move the operating fan point so that it was identical to that of the hover operating point. This would be ideal in terms of fan performance providing an efficiency of $\eta_{F,cr} = 0.88$. However, during cruise flight operations, the Lilium et is controlled via thrust vectoring and RPM adjustments of single or multiple fans, so a safe stall margin is required for the nominal cruise operating point to allow for off-design operation during manoeuvres. Closing the variable area nozzle also increases the jet velocity which reduces the overall system's propulsive efficiency. Taking these effects into account, the variable area nozzle area ratio for cruise can be optimised at a flow coefficient which is 0.3 higher by setting $\sigma_{cr} = 0.9$, which leads to $\phi_{real} = 1.31$, $\psi_{cr,real} = 0.27$ and a fan efficiency of $\eta_{F,cr} = 0.83$.

The design flow coefficient of the fan $\phi_h = 1.09$ is higher than those typically reported in the literature where the optimal flow coefficient is approximately $\phi = 0.6$. The choice of a high design flow coefficient is deliberate. It allows both the fan diameter to be kept low, and the blade tip Mach number to be below 0.45. This is especially important for reducing fan noise. High fidelity analysis, such as CFD and other advanced in-house analysis tools, give Lilium confidence

that ducted fans with high flow coefficients $\phi_{cr} = 1.31$ can be designed during cruise flight at efficiencies of $\eta_{F,cr} = 0.83$, while achieving peak performance in hover flight with a fan efficiency of $\eta_{F,h} = 0.88$.

There is little published literature on fans or compressors designed at these high flow coefficients. However, it is interesting to note that Howell (1945) tested the isentropic efficiency of a two-dimensional compressor blade with a design flow coefficient of $\phi = 1.0$ and measured a design isentropic efficiency of around $\eta_F = 88\%$ and retained an efficiency of above 85% up to a flow coefficient of around $\phi = 1.3$.

4.2.2. Propulsive efficiency

The propulsive efficiency in cruise η_P is defined as

$$\eta_P = \frac{\text{power to aircraft}}{\text{power from jet}} = \frac{v_{cr} \dot{m}_{cr} \cdot (v_{j,cr} - v_{cr})}{0.5 \cdot \dot{m}_{cr} \cdot (v_{j,cr}^2 - v_{cr}^2)} = \frac{2 \cdot v_{cr}}{v_{cr} + v_{j,cr}}, \quad (32)$$

where $v_{j,cr}$ is the jet velocity during cruise. Equation (32) is commonly known as the Froude equation.

The jet velocity in cruise $v_{j,cr}$ is calculated by applying the steady flow momentum equation to a control volume surrounding the propulsor, see Farokhi (2014); Eckert and Schnell (2013), and rearranging gives

$$v_{j,cr} = \frac{A_{j,cr,tot} \cdot \rho_{cr} \cdot v_{cr} + \sqrt{(A_{j,cr,tot} \cdot \rho_{cr} \cdot v_{cr})^2 + 4(A_{j,cr,tot} \cdot \rho_{cr} \cdot D_{cr})}}{2A_{j,cr,tot} \cdot \rho_{cr}} = 93.96m/s, \quad (33)$$

where $A_{j,cr,tot} = n \cdot \sigma_{cr} \cdot A_d$ is total jet area in cruise. Substituting Equation (33) in Equation (32) gives the propulsive cruise efficiency as

$$\eta_P = \frac{2 \cdot v_{cr}}{v_{cr} + v_{j,cr}} = 0.939. \quad (34)$$

4.2.3. Duct efficiency

The duct efficiency η_D accounts for losses in the boundary layer on the inside of the duct, shown by the red surfaces in Figure 4. The loss in the fan stage control volume has already been accounted for by the fan efficiency. The duct efficiency therefore accounts for the losses only in the part of the boundary layer outside of the fan stage control volume. For the duct efficiency η_D we further consider the effective length of the hub to be $l_{hub} = 0.5m$, see also Figure 4.

The duct efficiency is defined as

$$\eta_D = \frac{\text{power to jet}}{\text{power from flow}} = 1 - \frac{T\dot{S}_{d,irrev}}{0.5 \cdot \dot{m}_{cr} \cdot (v_{j,cr}^2 - v_{cr}^2) + T\dot{S}_{d,irrev}}, \quad (35)$$

where $T\dot{S}_{d,irrev}$ are the boundary layer losses in the duct due to viscous dissipation which can be calculated for the hover and cruise fan operating points as

$$T\dot{S}_{d,irrev} = n \cdot A_s \cdot C_D \cdot \rho \cdot v_d^3 = n \cdot (\pi(l_s - l_{stage}) \cdot (d_h + d_s)) \cdot C_D \cdot \rho (v_j \cdot \sigma)^3. \quad (36)$$

The dissipation coefficient of a turbulent boundary layer is set at $C_D = 0.002$, see Denton (1993). It should be noted that the dissipation coefficient of turbulent boundary layers is a relatively weak function of Reynolds number in the range of Reynolds numbers investigated and therefore may be considered constant.

The jet velocity $v_{j,cr}$ was calculated in the previous section for the cruise case as $v_{j,cr} = 94.11m/s$ and substituting this result into Equation (36) gives us

$$T\dot{S}_{d,irrev,cr} = 12.57kW, \quad (37)$$

which leads to a duct efficiency for the cruise case of

$$\eta_{D,cr} = 0.923. \quad (38)$$

For the hover case the procedure is repeated using the jet velocity $v_{j,h}$ for hover. This is derived from Equation (33) noting that the flight speed is zero and the thrust is the same as the weight of the aircraft. This yields a nozzle exit velocity of:

$$v_{j,h} = \sqrt{\frac{MTOM \cdot g}{\rho_h A_{j,h,tot}}} = 97.59m/s, \quad (39)$$

where the density $\rho_h = 1.225kg/m^3$ is defined by standard atmospheric conditions at sea level. $A_{j,h,tot} = n \cdot \sigma_h \cdot A_d$ is the total jet area in hover. The corresponding disc loading λ is:

$$\lambda = \frac{MTOM}{A_{d,h,tot}} = \frac{3,175kg}{2.67m^2} = 1,189 \frac{kg}{m^2}, \quad (40)$$

Substituting the results from Equation (39) into Equation (36), the duct loss at hover is calculated as:

$$T\dot{S}_{d,irrev,h} = 56.87kW, \quad (41)$$

giving a duct hover efficiency of

$$\eta_{D,h} = 0.964. \quad (42)$$

4.2.4. Motor efficiency

The motor efficiency η_M is defined as

$$\eta_M = \frac{\text{power to shaft}}{\text{power from motor}} \quad (43)$$

The motor efficiency in cruise is assumed to be $\eta_{M,cr} = 95\%$ and in hover $\eta_{M,h} = 92\%$. These are typical for commercially available motors. The variation between hover and cruise values arises from the heat losses caused by increased RPM in hover. The viability of these numbers is demonstrated and discussed in more detail in Section 5.2.

4.2.5. Power electronics efficiency

The power electronics efficiency η_{PE} is defined as

$$\eta_{PE} = \frac{\text{power to motor}}{\text{power from battery}} \quad (44)$$

The power electronics efficiency in cruise is assumed to be $\eta_{PE,cr} = 98\%$ and in hover $\eta_{PE,h} = 95\%$. The variation between hover and cruise values arises from heat losses caused by the increased power demand in hover.

4.2.6. Battery efficiency

The battery efficiency η_B is defined as

$$\eta_B = \frac{\text{electrical power from battery}}{\text{battery power}} \quad (45)$$

The battery efficiency in cruise is assumed to be $\eta_{B,cr} = 98\%$ and in hover $\eta_{B,h} = 80\%$. The variation between hover and cruise values arises from the losses due to increased power demand in hover, which leads to thermal losses and, thus, increased internal resistance leading to small battery efficiencies.

4.3. Power extraction from the battery

The power in each of the four modes of flight can now be calculated for the Lilium Jet.

4.3.1. Hover power

The hover power P_h is calculated using Equation(4) with a term P_{board} added for the additional power consumption of air conditioning and avionics during cruise flight.

$$P_h = \frac{\frac{1}{2} \frac{T_h^{3/2}}{\sqrt{\rho_h \cdot \eta \cdot A_{j,h}}}}{\eta_{F,h} \cdot \eta_{D,h} \cdot \eta_{PE,h} \cdot \eta_{M,h} \cdot \eta_{B,h}} + P_{board}, \quad (46)$$

where the overall aircraft efficiency during hover is $\eta_{0,h} = \eta_{F,h} \cdot \eta_{D,h} \cdot \eta_{PE,h} \cdot \eta_{M,h} \cdot \eta_{B,h} \approx 59\%$ and $P_{board} = 8kW$ through the whole flight. Substituting into equation (46) gives

$$P_h = 2,570kW. \quad (47)$$

It is an interesting academic question to calculate maximum hover time which the power in Equation (46) and the total battery energy in Equation (1) would allow.

$$t_h^{max} = \frac{E_s \cdot (1 - SOC_{min})}{P_h} = 384s. \quad (48)$$

It should, however, be noted that this hover time would in practice be impossible because it would lead to overheating of the battery packs.

4.3.2. Cruise power

The cruise power P_{cr} is calculated with Equation (8) where once again P_{board} is added for the additional power consumption of air conditioning and avionics during cruise flight as

$$P_{cr} = \frac{\sum_i D_{i,cr} \cdot v_{cr}}{\eta_{P,cr} \cdot \eta_{D,cr} \cdot \eta_{F,cr} \cdot \eta_{PE,cr} \cdot \eta_{M,cr} \cdot \eta_{B,cr}} + P_{board}. \quad (49)$$

The aircraft's cruise efficiency is $\eta_{0,cr} = \eta_{P,cr} \cdot \eta_{D,cr} \cdot \eta_{F,cr} \cdot \eta_{PE,cr} \cdot \eta_{M,cr} \cdot \eta_{B,cr} \approx 65\%$. Substituting into Equation (49) gives

$$P_{cr} = 224kW. \quad (50)$$

4.3.3. Transition power

The transition power P_{tr} is calculated with Equation (9)

$$P_{tr,avg} = \frac{(P_h + P_{tr,eff})}{2} + P_{board}. \quad (51)$$

where $P_{tr,eff} = P_h/10$. Substituting into Equation (51) gives

$$P_{tr,avg} = 1,421kW. \quad (52)$$

4.3.4. Climbing power

The climb power P_{cl} is calculated from Equation (10) as

$$P_{cl} = \frac{(\sum_i D_{i,cl} + MTOM \cdot g \cdot \sin(\Phi)) \cdot v_{cl}}{\eta_{P,cl} \cdot \eta_{D,cl} \cdot \eta_{F,cl} \cdot \eta_{PE,cl} \cdot \eta_{M,cl} \cdot \eta_{B,cl}} + P_{board}. \quad (53)$$

During climb, we set the climb angle to $\Phi = 5^\circ$. This means that the thrust of the aircraft has to overcome both the aircraft's drag and a component of its weight. This results in the power in climb being around twice the power in cruise. As discussed earlier, during climb the altitude increases to 3000m and

the speed raises to $v_{cr} = 300km/h$. This means that the power changes through the climb phase. However, in practice this change is not large and for simplicity a mean altitude of 1500m with a mean climb velocity $v_{cl} = 275km/h$ is set. Taking the drag value from Table 2, the climb drag is

$$D_{cl} = 1,698N. \quad (54)$$

The jet velocity in climb is higher than in cruise because the thrust of the propulsion system must overcome both the drag and a component of the weight. This means that the propulsive efficiency of the aircraft and duct efficiency must be recalculated. The final values of the drag and efficiencies used in the climb calculation are shown in Table 2. Substituting in (53) gives

$$P_{cl} = 511kW. \quad (55)$$

The comparison between Equation (55) and Equation (50) reveals that the climbing power is around a fifth of the hover power. This demonstrates the benefit of the DVTC architecture on RAM missions.

The descent power P_{des} is calculated from Equation (11) as

$$P_{des} = 0.2 \cdot P_{cr} + P_{board} = 52.88kW. \quad (56)$$

As discussed earlier, during the descent, the component of the aircraft weight switches direction. To ensure a powered descent the engines are operated during the descent phase of the flight at 20% of the cruise power.

4.4. Aircraft range

Having calculated the power demand for each phase of flight we can now calculate the aircraft range. The simplified mission, shown in Figure 3, is used. The time of each of the seven phases of the flight are shown in Table 3. Substi-

Phase of flight	Time (seconds)
Take-off hover	15
Transition	21.2
Climb	451
Cruise	t_{cr}
Descent	451
Re-transition	21.2
Landing hover	45

Table 3: Duration for each phase of the simplified mission.

tuting into Equation (14) gives a range

$$R = \frac{v_{cr}}{P_{cr}}(E_s(1 - SOC_{min}) - t_h \cdot P_h - 2 \cdot t_{tr} \cdot P_{tr} - t_{cl} \cdot (P_{cl} + P_{des})) + 2 \cdot t_{cl} \cdot v_{cl} = 261km. \quad (57)$$

The focus of this paper has been on providing a simplified method of calculating the realistic maximum range of a DVTC e-VTOL aircraft. The analysis shows that for the DVTC e-VTOL aircraft considered this is $R = 261km$. The result demonstrates that the aircraft is suitable for RAM markets.

The range obtained assumes that all of the available battery energy is consumed. For an operational aircraft, pre-planned operational manoeuvres e.g., diverts or emergency procedures, will also need to be accounted for. Discussion with authorities on these pre-planned operational manoeuvres are ongoing. However, the operational mission planning framework for e-VTOL aircraft is not expected to be based on a percentage of total onboard energy since the diversity of e-VTOL concepts would lead to inconsistent reserve planning. Instead missions are likely to include absolute reserve planning, meaning that a range above 200km is realistic for aircraft similar to the one presented in this paper.

4.5. First order noise assessment

Though the aim of this paper is to analyse the range of the aircraft it is also important to comment on it's noise emissions while in hover flight. In this analysis only the far field propagation is considered. This is because it is the most important noise component for the proposed inner city flight operation.

Following a standard procedure as described by Schieber (2021), the aircraft overall sound pressure level L_{ac} at an arbitrary distance R_{ac} can be calculated as

$$L_{ac} = L_{eng} + 10 \log_{10}(n) - L_{atm}(R_{ac}) - 20 \log_{10}\left(\frac{R_{ac}}{R_{eng}}\right), \quad (58)$$

where L_{eng} is the overall sound pressure level correlated at a distance of $R_{eng} = 1m$ from a single engine. n is the number of ducted fans per aircraft, and $R_{ac} = 100m$ is the reference distance from the take-off pad, representative of the location where an observer is located. For the frequency integrated atmospheric correction L_{atm} we use the method found by Rickley et al. (2007).

In order to approximate L_{eng} for any axial ducted fan, the NASA source diagnostic test (STD) described among others by the Regenscheit analogy in VDI (1982) is used. Using the engine geometry described in Section 2, we calculate $L_{eng} = 94dB(A)$ at $R_{eng} = 1m$. Substituting into Equation (59) the aircraft overall sound pressure level L_{ac} at a distance of $R_{ac} = 100m$ gives $L_{ac} = 65dB(A)$. The Regenscheit analogy has a standard deviation of $\pm 2.7dB(A)$. This low noise emission is the result of the fan being located in

a duct and to the tip speed of the blade being limited to $u_{b,tip} = 154.38m/s$, which is equivalent to a Mach number $Ma = 0.45$, see also Appendix B.

In addition, acoustic liners are included in the duct. These are designed to reduce tonal noise through Helmholtz and porous liners. Sutliff (2019) and Aurégan (2018) show that in small ducted fans these reduce noise by $\approx 1dB(A)$ for every centimeter of liner length. This has the effect of significantly reducing tone noise from the noise spectrum, and thus, reduces the overall engine noise. With the acoustic liners in place we calculate the overall sound power will be reduced to $L_{eng} = 89dB(A)$ at $R_{eng} = 1m$. Substituting into Equation (59) the aircraft overall sound pressure level L_{ac} at a distance of $R_{ac} = 100m$ drops to $L_{ac} = 60.6dB(A)$.

Finally, the ducted fan configuration allows noise attenuation techniques through blade design, e.g. by the used of swept rotors and stators, Envia and Nallasamy (1999). In this assessment it is assumed that this can be used to further reduce the aircraft overall sound pressure level below

$$L_{ac} < 60.0dB(A), \quad (59)$$

at $R_{ac} = 100m$ for the real aircraft. This is equivalent to the sound level created by normal conversation. Finally, for reference, in cruise, due to lower thrust, the aircraft's overall sound pressure level L_{ac} at a distance of $R_{ac} = 100m$ is $L_{ac,cr} = 54.4dB(A)$.

Based on first order assumptions and applying standard industry tools during the architecture design phase, Lilium believe that the inner city operation of a 7-seat, 3,175kg e-VTOL aircraft can be below $L_{target} < 60dB(A)$ at a distance of 100m.

5. Technology assessment

5.1. Battery technology development

E-VTOL aircraft typically utilise Lithium-Ion batteries and since 2014 these have been commercially available with energy densities of $e_b = 250Wh/kg$, e.g. the LG HG2 battery described in Chorong (2015). The concept presented in this paper assumes $e_b = 320Wh/kg$, see Section 2. This choice was based on demonstrations of the state-of-the-art battery capabilities by leading industry players. Research into improving battery-based energy storage is being driven by suppliers looking to enter the UAM and RAM markets. A number of publications have reported Lithium-Ion batteries with energy densities at around $320Wh/kg$. Lin et al. (2017) reported energy densities in excess of $320Wh/kg$. Shirk and Chinh (2020), and QuantumScape, see Singh (2020), reported battery cells capable of energy densities in excess of $320Wh/kg$ with standard cathode materials. Zenlabs (2021) reported battery cells with $e_b = 315Wh/kg$ while achieving 1000 charge-discharge cycles. Stefan (2019) reported energy densities

in excess of $350Wh/kg$ by using different anode materials.

In addition active research is underway in the development of solid-state batteries. Singh (2020) predicts that these will be commercially available within 5 years with an energy density in excess of $400Wh/kg$.

The specific power required during short periods of hover, reported in Section 4.3, is $P_h/m_b = 2.7kW/kg$. The cell family introduced by Shirk and Chinh (2020), demonstrates that a constant specific power beyond $2kW/kg$ can be achieved with $e_b \approx 300Wh/kg$. Beyond that, they demonstrate the ability to deliver constant high power and high energy densities, while allowing the batteries to be discharged to $SOC_{min} = 10\%$. A value of $SOC_{min} = 10\%$ is therefore used in this paper.

5.2. Powertrain and electric motor efficiencies

The motor efficiency is assumed to be $\eta_{M,h} = 92\%$, $\eta_{M,cr} = 95\%$ and $\eta_{M,cl} = 95\%$ and the power electronics efficiency to be $\eta_{PE,h} = 95\%$, $\eta_{PE,cr} = 98\%$ and $\eta_{PE,cl} = 98\%$ in hover, cruise and climb phases respectively.

These values are available for devices commercially available from aerospace suppliers. These assumptions are supported by Seitz et al. (2012), where overall electric system efficiencies of greater than 90% are reported.

6. Parameter variation analysis

In this section, the effect on range of the batteries energy density, hover time and the ratio of battery mass to payload are studied. These parameters are chosen as they have the largest impact on range and are most likely to affect how the aircraft is operated in the near future. Aerodynamic, powertrain, motor and battery efficiencies are fixed for this analysis as technological development in these areas is expected to be incremental. Five variations from the concept described in the previous sections (DVTC-1) are considered and the results are shown in Table 4.

DVTC-1: DVTC-1a is the reference concept, with a range of $R = 261km$.

DVTC-2: The battery cells energy density is assumed to be of $e_B = 250Wh/kg$, based on technology commercially available since 2014, see Section 5.1. With all other assumptions fixed the range drops to $180km$. This shows that even with commercially available batteries the aircraft can service a significant RAM market.

DVTC-3: The total operating hover time is increased from $t_h = 60s$ to $t_h = 90s$. With all other assumptions fixed, including $e_B = 320Wh/kg$, the range drops to $R = 232km$. This highlights an important observation that DVTC aircraft

Aircraft variation	Input			Range
	$e_B [Wh/kg]$	$t_h [s]$	$\mu_b/\mu_{pl} [-]$	$R [km]$ (Section 4.4)
DVTC-1	320	60	1.36	261
DVTC-2	250	60	1.36	181
DVTC-3	320	90	1.36	232
DVTC-4	400	60	1.36	353
DVTC-5a	320	60	2.30	337
DVTC-5b	400	60	2.30	448

Table 4: Parameter variation for an investigated e-VTOL aircraft architecture. All range values and hover times are calculated for a minimum acceptable state-of-charge of $SOC_{min} = 10\%$.

with relatively highly loaded ducted fans should be designed for as little hover time as possible to exploit the cruise efficiency.

DVTC-4: The battery cells energy density is assumed to be of $e_b = 400Wh/kg$, based on future solid state battery capability, discussed in Section 5.1. With all other assumptions fixed the range increases to $R = 353km$. This means that even accounting for operational reserves, markets with ranges in excess of $R > 300km$ could be served.

DVTC-5a: This version examines the trade-off between battery mass, payload and range by configuring DVTC-5a as a 5-seat aircraft instead of a 7-seater. The payload, m_{pl} is reduced by $200kg$ so that battery mass, m_b is increased by $200kg$ and, thus, μ_b/μ_{pl} increases from 1.36 to 2.30. The battery energy density for this version is set to $e_B = 320Wh/kg$. This change in configuration is not expected to effect the other assumptions presented in this paper and the range is calculated as $R = 337km$.

DVTC-5b: DVTC-5b is a 5-seat aircraft, similar to DVTC-5a, with the only difference being the use of battery technology with an energy density of $e_B = 400Wh/kg$. The extra energy available increases the maximum range of DVTC-5b to $R = 448km$ meaning that markets with ranges in excess of $R > 400km$ could be served with this concept.

7. Conclusion

The aim of this paper is to demonstrate the technical feasibility of a Ducted Vectored Thrust Concept (DVTC) as an electric vertical take-off and landing (e-VTOL) aircraft in both the urban and regional air mobility (UAM / RAM) markets. We describe the specification of an aircraft architecture based on the Lilium jet and define a mission suitable for the regional air mobility market. A simplified methodology of analysis is applied which allows a range to be calculated accurately while retaining enough simplicity to allow the reader to gain a

physical understanding of the key trades.

The analysis shows that if an available battery technology with energy density of $320Wh/kg$ is assumed then the 7-seater DVTC aircraft with a maximum take-off mass of $3,175kg$ can achieve a range of $261km$. It is shown that the development of solid-state batteries with an energy density in excess of $400Wh/kg$ would increase the range of the aircraft beyond $330km$.

The range was assessed without operational penalties being considered. However, it is believed that inclusion of all necessary reserves will still allow an aircraft with a range greater than $200km$ allowing significant business opportunities in the RAM markets.

The analysis shows that noise levels of less than $60dB(A)$ at an observe distance of $100m$, are feasible during hover. This is equivalent to the sound level created by normal conversation.

In conclusion, the Ducted Vectored Thrust Concept (DVTC) can be designed with much higher disc loading than a propeller aircraft with the same noise emission. Heavier aircraft with higher payload can be achieved at a reduced footprint compared to open rotor concepts, while keeping noise emissions low through the use of acoustic liners.

References

- Y. Aurégan. Ultra-thin low frequency perfect sound absorber with high ratio of active area. *Applied Physics Letters*, 113:201904, 11 2018. doi: 10.1063/1.5063504.
- A. Bacchini and E. Cestino. Electric vtol configurations comparison. *Aerospace*, 6, 2019. doi: <https://doi.org/10.3390/aerospace6030026>.
- W. Bittner. *Flugmechanik der Hubschrauber*. Springer-Verlag, 2nd edition, 2005. doi: <https://doi.org/10.1007/3-540-27541-X>.
- M. P. Boyce. *Preface to the First Edition*. Butterworth-Heinemann, Oxford, fourth edition edition, 2012. ISBN 978-0-12-383842-1. doi: <https://doi.org/10.1016/B978-0-12-383842-1.00043-3>. URL <https://www.sciencedirect.com/science/article/pii/B9780123838421000433>.
- S. S. Chauhan and J. R. R. A. Martins. Tilt-wing evtol takeoff trajectory optimization. *Journal of Aircraft*, 57(1):93–112, 2020. doi: 10.2514/1.C035476. URL <https://doi.org/10.2514/1.C035476>.
- S. Chorong. Product specification. <https://www.batteryspace.com/prod-specs/9989.specs.pdf>, 2015. Accessed: 2021-02-21.

- M. Clarke, J. Smart, E. M. Botero, W. Maier, and J. J. Alonso. *Strategies for Posing a Well-Defined Problem for Urban Air Mobility Vehicles*. 2019. doi: 10.2514/6.2019-0818. URL <https://arc.aiaa.org/doi/abs/10.2514/6.2019-0818>.
- J. D. Denton. *Loss Mechanisms in Turbomachines*, volume Volume 2: Combustion and Fuels; Oil and Gas Applications; Cycle Innovations; Heat Transfer; Electric Power; Industrial and Cogeneration; Ceramics; Structures and Dynamics; Controls, Diagnostics and Instrumentation; IGTI Scholar Award of *Turbo Expo: Power for Land, Sea, and Air*. 05 1993. doi: 10.1115/93-GT-435. URL <https://doi.org/10.1115/93-GT-435>. V002T14A001.
- C. E. Dole, J. E. Lewis, J. B. Badick, and B. A. Johnson. *Flight Theory and Aerodynamics: A Practical Guide for Operational Safety*. Wiley, 3rd edition, 2016.
- EASA. Special condition for small-category VTOL aircraft. <https://www.easa.europa.eu/sites/default/files/dfu/SC-VTOL-01.pdf>, 2019.
- B. Eckert and E. Schnell. *Axial- und Radialkompressoren: Anwendung/Theorie/Berechnung*. Springer-Verlag, 2nd edition, 2013.
- E. Envia and M. Nallasamy. Design selection and analysis of a swept and leaned stator concept. *Journal of Sound and Vibration*, 228(4):793 – 836, 1999. ISSN 0022-460X. doi: <https://doi.org/10.1006/jsvi.1999.2441>. URL <http://www.sciencedirect.com/science/article/pii/S0022460X99924410>.
- S. Farokhi. *Aircraft Propulsion*. Wiley, 2nd edition, 2014.
- N. Gourdain. Prediction of the unsteady turbulent flow in an axial compressor stage. part 1: Comparison of unsteady rans and les with experiments. *Computers & Fluids*, 106:119 – 129, 2015. ISSN 0045-7930. doi: <https://doi.org/10.1016/j.compfluid.2014.09.052>. URL <http://www.sciencedirect.com/science/article/pii/S0045793014004022>.
- C. A. Hall and D. Crichton. Engine Design Studies for a Silent Aircraft. *Journal of Turbomachinery*, 129(3):479–487, 07 2006. ISSN 0889-504X. doi: 10.1115/1.2472398. URL <https://doi.org/10.1115/1.2472398>.
- E. S. Hendricks, R. D. Falck, J. S. Gray, E. Aretskin-Hariton, D. Ingraham, J. W. Chapman, S. L. Schnulo, J. Chin, J. P. Jasa, and J. D. Bergeson. *Multidisciplinary Optimization of a Turboelectric Tiltwing Urban Air Mobility Aircraft*. 2019. doi: 10.2514/6.2019-3551. URL <https://arc.aiaa.org/doi/abs/10.2514/6.2019-3551>.
- A. R. Howell. Fluid dynamics of axial compressors. *Proceedings of the Institution of Mechanical Engineers*, 153(1):441–452, 1945. doi: 10.1243/PIME\PROC\1945\153\049\02. URL https://doi.org/10.1243/PIME_PROC_1945_153_049_02.

- H. D. Kim, A. T. Perry, and P. J. Ansell. *A Review of Distributed Electric Propulsion Concepts for Air Vehicle Technology*. 2018. doi: 10.2514/6.2018-4998. URL <https://arc.aiaa.org/doi/abs/10.2514/6.2018-4998>.
- S. Kim, D. Kim, C. Son, K. Kim, M. Kim, and S. Min. A full engine cycle analysis of a turbofan engine for optimum scheduling of variable guide vanes. *Aerospace Science and Technology*, 47:21 – 30, 2015. ISSN 1270-9638. doi: <https://doi.org/10.1016/j.ast.2015.09.007>. URL <http://www.sciencedirect.com/science/article/pii/S1270963815002655>.
- I. Kroo. Drag due to lift: Concepts for prediction and reduction. *Annual Review of Fluid Mechanics*, 33(1):587–617, 2001. doi: 10.1146/annurev.fluid.33.1.587.
- I. M. Kroo. Minimum induced drag of canard configurations. *Journal of Aircraft*, 19(9):792–794, 1982. doi: 10.2514/3.61557.
- D. Kuchemann. *The Aerodynamic Design of Aircraft*. American Institute of Aeronautics and Astronautics (AIAA) Education Series, 2012.
- Lilium. The Lilium jet technology. <https://lilium.com/the-jet>, 2019a.
- Lilium. Visual representation of the planform area of the Lilium jet. <https://photos.app.goo.gl/ozik5SJcpsQE8fdQ7>, 2019b.
- D. Lin, Y. Liu, and Y. Cui. Reviving the lithium metal anode for high-energy batteries. *Nature Nanotechnology*, 12(3):194–206, 2017. doi: 10.1038/nnano.2017.16. URL <https://doi.org/10.1038/nnano.2017.16>.
- F. Nicolosi, P. Vecchia, D. Ciliberti, and V. Cusati. Fuselage aerodynamic drag prediction method by cfd. 09 2015.
- M. T. Pascu. *Modern Layout and Design Strategy for Axial Fans*. doctoralthesis, Friedrich-Alexander-Universität Erlangen-Nürnberg (FAU), 2009.
- C. Pitis. Energy efficient single stage axial fan (enef). pages 280 – 285, 11 2007. ISBN 978-1-4244-1444-4. doi: 10.1109/EPC.2007.4520343.
- N. Polaczyk. A review of current technology and research in urban on-demand air mobility applications. 2019. URL <https://repository.tudelft.nl/islandora/object/uuid:10d1c68a-dfb9-4419-a912-26e6c1742853?collection=research>.
- P. Pradeep and P. Wei. Energy-efficient arrival with rta constraint for multirotor evtol in urban air mobility. *Journal of Aerospace Information Systems*, 16(7): 263–277, 2019. doi: 10.2514/1.1010710. URL <https://doi.org/10.2514/1.1010710>.
- E. J. Rickley, G. G. Fleming, and C. J. Roof. Simplified procedure for computing the absorption of sound by the atmosphere. *Noise Control Engineering Journal*, 55(6):482–494, 2007. doi: <https://doi.org/10.3397/1.2820987>. URL <https://www.ingentaconnect.com/content/ince/ncej/2007/00000055/00000006/art00001>.

- F. Schieber. Procedure for Estimating the Combined Noise Level of Multiple Acoustic Sources. 2021. URL <http://apps.usd.edu/coglab/schieber/psyc707/pdf/AddedNoiseLevels.pdf>.
- H. Schlichting and E. A. Truckenbrodt. *Aerodynamik des Flugzeuges: Erster Band: Grundlagen aus der Strömungstechnik Aerodynamik des Tragflügels (Teil I)*. Springer-Verlag, 3rd edition, 2001a.
- H. Schlichting and E. A. Truckenbrodt. *Aerodynamik des Flugzeuges: Zweiter Band: Aerodynamik des Tragflügels (Teil II), des Rumpfes, der Flügel-Rumpf-Anordnung und der Leitwerke*. Springer-Verlag, 3rd edition, 2001b.
- A. Seitz, O. Schmitz, A. Isikveren, and M. Hornung. Electrically powered propulsion: Comparison and contrast to gas turbines. 09 2012.
- M. Shirk and H. Chinh. Cuberg hp-5p cells (incl p500). https://www.cuberg.net/media/DOE_results_for_Cuberg.pdf, 2020.
- J. Singh. Next-generation solid-state batteries. https://s26.q4cdn.com/263384136/files/doc_presentation/2020/12/QS-Data-Launch-2020_12.08.pdf, 2020.
- J. H. Spurk and N. Aksel. *A Physical Introduction to Fluid Mechanics*. Springer-Verlag, 3rd edition, 2019.
- I. Stefan. High energy density and specific energy batteries with silicon anodes. <https://www.metalbulletin.com/events/download.ashx/document/speaker/E001854/a0I1t00000I5R1SEAV/Presentation>, 2019.
- D. L. Sutliff. *A 20 Year Retrospective of The Advanced Noise Control Fan – Contributions to Turbofan Noise Research*. 2019. doi: 10.2514/6.2019-3824. URL <https://arc.aiaa.org/doi/abs/10.2514/6.2019-3824>.
- D. P. Thipphavong, R. Apaza, B. Barmore, V. Battiste, B. Burian, Q. Dao, M. Feary, S. Go, K. H. Goodrich, J. Homola, H. R. Idris, P. H. Kopardekar, J. B. Lachter, N. A. Neogi, H. K. Ng, R. M. Oseguera-Lohr, M. D. Patterson, and S. A. Verma. *Urban Air Mobility Airspace Integration Concepts and Considerations*. 2018. doi: 10.2514/6.2018-3676. URL <https://arc.aiaa.org/doi/abs/10.2514/6.2018-3676>.
- M. Trancossi and M. Madonia. The efficiency of an electric turbofan vs. inlet area: A simple mathematical model and cfd simulations. *SAE Technical Papers*, 10, 10 2012. doi: 10.4271/2012-01-2217.
- VDI. *VDI 3731 Blatt 1 - Normenausschuss Akustik, Lärmmin-derung und Schwingungstechnik (NALS) im DIN und VDI: Characteristic noise emission values of technical sound sources; compressors*. 12 1982. URL <https://www.vdi.de/richtlinien/details/vdi-3731-blatt-1-emissionskennwerte-technischer-schallquellen-kompressoren>.

- R. Whittle. Air mobility bonanza beckons electric vtol developers. <https://pdfs.semanticscholar.org/a132/ba1a11012da261627597f1d074c3f3ea67e9.pdf>, 2018. Accessed: 2010-09-30.
- X. Ye, P. Li, and C. Li. Numerical investigation of grooved blade tips effect on the performance of an axial flow fan. *Zhongguo Dianji Gongcheng Xuebao/Proceedings of the Chinese Society of Electrical Engineering*, 35:652–659, 2015. doi: 10.13334/j.0258-8013.pcsee.2015.03.019.
- E. Zenlabs. Idaho national laboratory validates 1000 charge-discharge cycles from zenlabs’ silicon anode-based lithium-ion cells. 2021. URL <https://www.prnewswire.com/news-releases/idaho-national-laboratory-validates-1000-charge-discharge-cycles-from-zenlabs-silicon-anode-based-lithium-ion-cells-301226389.html>.

Appendix A. Hover thrust calculation

The power of the jet in hover is

$$P_j = 0.5 \cdot \dot{m}_h \cdot v_{j,h}^2. \quad (\text{A.1})$$

Applying the steady flow momentum equation to the ducted fan, the total thrust can be shown to be equal to the momentum flux of the exit jet

$$T_h = \dot{m}_h \cdot v_{j,h} = \rho_h \cdot A_{j,h} \cdot v_{j,h}^2. \quad (\text{A.2})$$

Substitution Equation (A.2) into Equation (A.1) gives an equation of the power of the jet in hover

$$P_j = 0.5 \cdot \rho_h \cdot A_{j,h} \cdot v_{j,h}^3 = \frac{T_h}{2} \sqrt{\frac{T_h}{\rho_h A_{j,h}}} = \frac{1}{2} \frac{T_h^{3/2}}{\sqrt{\rho_h A_{j,h}}}. \quad (\text{A.3})$$

In hover the thrust must be equal to the aircraft weight

$$T_{h,tot} = MTOM \cdot g. \quad (\text{A.4})$$

This allows the power of the jet in hover to be written as

$$P_j = 0.5 \cdot \rho_h \cdot A_{j,h} \cdot v_{j,h}^3 = \frac{1}{2} \frac{(MTOM \cdot g)^{3/2}}{\sqrt{\rho_h \cdot n \cdot A_{j,h}}}. \quad (\text{A.5})$$

The jet area of a single engine $A_{j,h} = A_d \cdot \sigma_h$ and total jet area of the n ducted fans $A_{j,h,tot}$ during hover flight is calculated from

$$A_{j,h} = \frac{(d_s^2 - d_h^2)}{4} \pi \cdot \sigma_h = 0.0742m^2 \quad A_{j,h,tot} = A_{d,h} \cdot n = 2.67m^2. \quad (\text{A.6})$$

Equation (A.3) differs from the power consumption for open rotor systems $P_{h,ideal}^{open}$

$$P_h^{open} = \frac{T_h^{3/2}}{\sqrt{2\rho_h A_{d,tot}}}, \quad (\text{A.7})$$

see Bittner (2005).

Appendix B. Fan design

The fan flow parameters for hover, cruise and climb are shown in Table B.5 and B.6. The fan calculation was undertaken at the mean radius r_m , which is the radius which represents 50% mass flow.

$$r_m = \sqrt{\frac{\left(\frac{d_s}{2}\right)^2 + \left(\frac{d_h}{2}\right)^2}{2}}. \quad (\text{B.1})$$

For the hover condition, $u_{b,mean}$ is fixed by the requirement, for noise reasons, that the maximum rotor blade tip Mach number $M_{b,tip} = 0.45$ resulting in $u_{b,mean} = 116.9m/s$.

At cruise and climb operating conditions the fan speed is set by the thrust, flight speed and the requirement that the cruise operating point lies on the fan characteristic shown in Figure 6. The relationship between stage loading and flow coefficient is approximated by

$$\psi = 1 + \phi \tan(\beta_2), \quad (\text{B.2})$$

where β_2 is the rotor exit flow angle in the relative frame. β_2 is fixed once ϕ and ψ in hover are specified by selecting the blade speed and is always negative. At any point on the characteristic, Equation (B.2) can be rewritten as

$$\frac{\Delta h_0}{u_{in}^2} = \frac{u_{j,\alpha}^2 - v_\alpha^2}{2 \cdot \eta_{F,\alpha} u_{b,mean}^2} = 1 + \frac{u_{in,\alpha}}{u_{b,mean,\alpha}} \tan(\beta_2), \quad (\text{B.3})$$

where $\eta_{F,\alpha}$ is the fan efficiency at operating condition α (hover \star_h or cruise \star_{cr}). Equation B.3 can be rearranged to a quadratic equation in $u_{b,mean}$ and this can be solved to give

$$u_{b,mean,\alpha} = \frac{-u_{in,\alpha} \tan(\beta_2) \sqrt{(u_{in,\alpha} \cdot \tan(\beta_2))^2 - \frac{2}{\eta_F} (v_\alpha^2 - (u_{j,\alpha}^{out})^2)}}{2}. \quad (\text{B.4})$$

The values of $u_{b,mean}$ for cruise and climb are shown in the final column of Table B.5 and this is used to calculate the non-dimensional parameters in Table B.6. The Reynolds number given in Table B.6 is defined as

$$Re_r = \frac{u_{b,mean} \cdot c_r}{\nu}, \quad (\text{B.5})$$

where the rotor chord length is $c_r = 0.052m$. The demonstrated procedure can be repeated for different radial cuts, but doesn't change the architectural decision making process.

	P_{shaft}	\dot{m}	u_j	v_{in}	Δh_0	$u_{b,mean}$
Hover	47.98kW	8.65kg/s	97.59m/s	126.87m/s	5.41kJ/kg	116.86m/s
Cruise	5.06kW	4.39kg/s	94.11m/s	84.69m/s	1.15kJ/kg	64.85m/s
Climb	12.21kW	5.42kg/s	98.98m/s	89.08m/s	2.77kJ/kg	78.29m/s

Table B.5: Fan flow parameters. Values provided per fan.

	ϕ	ψ	Re_r	$M_{b,tip}$
Hover	1.085	0.396	610,415	0.45
Cruise	1.306	0.273	280,434	0.26
Climb	1.138	0.367	365,760	0.31

Table B.6: Non-dimensional fan operating points.

For low pressure ratio fans with similar aerodynamic parameters, isentropic stage efficiencies exceeding $\eta_{aero}^{engine} > 0.9$ have been reported and validated in Boyce (2012); Gourdain (2015); Ye et al. (2015); Kim et al. (2015); Pascu (2009); Pitis (2007) and, thus, we set $\eta_{F,h} = 0.88$.

Appendix C. List of abbreviation and symbols

Abbreviation	Description
DEP	Distributed Electric Propulsion
DVTC	Ducted Vectored Thrust Concept
e-VTOL	Electric vertical take-off and landing
FATO	Final approach and take-off areas
MTOM	Maximum take-off mass
RAM	Regional air mobility
RPM	Revolutions per minute
SOC	State of charge
UAM	Urban air mobility
Symbol	Description
A_d	Disc area of ducted fans
$A_{j,\alpha}$	Effective jet area of a ducted fan
$A_{j,\alpha,tot}$	Effective jet area of all ducted fans
$A_{flap,o}$	Surface area without shroud surface
C	Idealized compressor characteristic
C_D	Drag coefficient
$C_{D,c}$	Cabin drag coefficient in cruise flight
$C_{D,f}$	Flap drag coefficient in cruise flight
$C_{D,w}$	Wing drag coefficient in cruise flight
c_r	Rotor chord length
$c_{u,2}$	Post rotor circumferential velocity

D_{cr}	Total drag in cruise flight
D_c	Total cabin drag in cruise flight
$D_{c,ideal}$	Ideal cabin drag in cruise flight
D_f	Total flap drag in cruise flight
D_i	Induced drag in cruise flight
D_w	Total wing drag in cruise flight
d_h	Hub diameter
d_s	Shroud diameter
E_{acc}	Accessible energy in the battery
E_s	Total stored energy in the battery
e	Oswald factor
e_b	Energy density of batteries
g	Gravitational acceleration $g = 9.81m/s^2$
Δh_0	Enthalpie increase over the stage
l_b	Length of cabin
h_c	Height of cabin
L_{ac}	Aircraft overall sound pressure level
$L_{ac,cr}$	Aircraft overall sound pressure level during cruise flight
L_{atm}	Atmospheric noise correction
L_{eng}	Sound pressure level correlated at a reference distance
L_{target}	Target overall sound pressure level in 100m distance
l_s	Shroud length
l_{stage}	Fan stage length
l_c	Chord length
Ma	Mach number
$Ma_{b,tip,\alpha}$	Mach number at the blade tip for the respective flight state
\dot{m}_α	Mass flow through the ducts in the respective flight state
m_b	Mass of batteries
m_{pax}	Passenger mass
m_p	Pilot mass
m_{pl}	Total payload
m_s	Empty aircraft mass
n	Total amount of engines
n_c	Engines on canard wing
n_w	Engines on main wing
P_{board}	Total power required for onboard systems
P_{cl}	Total power required during climb flight
P_{cr}	Total power required during cruise flight
P_{des}	Total power required during descent flight
P_h	Ideal power required during hover flight
$P_{tr,eff}$	Approximate power demand after transition phase
$P_{tr,avg}$	Average power demand during transition phase
R_{ac}	Arbitrary distance from aircraft
R_{min}	Minimal expected range for RAM
R_r	Average Reynolds number based on rotor
R_s	Average Reynolds number based on stator
$R_{r,\alpha}$	Reynolds number on the rotor stage for the respective flight state
$S_{c,\emptyset}$	Frontal surface area of the fuselage
U	RPM of the rotor stage
u_1	Circumferential blade velocity
$u_{1,tip}$	Circumferential blade velocity at blade tip
$v_{in,\alpha}$	Average inlet velocity before the fan stage
$u_{b,mean}$	Average blade velocity
r_{mean}	Mass averaged radius of the ducted fan
S_w	Total main wing reference area
s_w	Main wing span
s_c	Canard span

T_α	Total thrust required during the respective flight state
$T\dot{S}_{d,irrev,\alpha}$	Total losses due to viscous dissipation
t_{cl}	Operational climb time
t_{cr}	Operational cruise time
t_h^{max}	Theoretical maximum hover time
t_h	Total hover time
$t_{h,l}$	Operational hover time during landing
$t_{h,to}$	Operational hover time during take-off
t_{tr}	Operational transition time
\dot{V}	Volume flow in ducted fan
v_{cl}	Average climb velocity
v_{cr}	Cruise velocity
$v_{d,\alpha}$	Flow velocity in fan duct
$v_{j,\alpha}$	Nozzle exit velocity
v_{cl}	Total climb path velocity
$v_{v,cl}$	Vertical climb velocity
w_c	Width of cabin
Greek symbols	Description
α	$\alpha = cr$ for cruise, $\alpha = cl$ for climb and $\alpha = h$ for hover respectively
$\eta_{0,\alpha}$	Total efficiency of the aircraft during the respective flight state
$\eta_{B,\alpha}$	Battery efficiency of the aircraft during the respective flight state
$\eta_{PE,\alpha}$	Power electronics efficiency of the aircraft during the respective flight state
$\eta_{M,\alpha}$	Motor efficiency of the aircraft during the respective flight state
$\eta_{F,\alpha}$	Fan efficiency of the aircraft during the respective flight state
$\eta_{D,\alpha}$	Duct efficiency of the aircraft during the respective flight state
$\eta_{P,\alpha}$	Propulsive efficiency of the aircraft during the respective flight state
κ	Power ratio between hover and the end of transition phase
Λ	Wing aspect ratio
λ	Disc loading
μ_b	Mass fraction of batteries
μ_{pl}	Mass fraction of payload
μ_s	Empty mass fraction of aircraft
ν	Air viscosity under atmospheric standard conditions at sea level
Φ	Climb angle
ϕ	Flow coefficient
ϕ_α	Flow coefficient during the respective flight state
$\phi_{\alpha,real}$	Effective flow coefficient during the respective flight state
ψ_α	Stage loading coefficient during the respective flight state
$\psi_{\alpha,real}$	Effective stage loading coefficient during the respective flight state
Ω	Glide ratio
ρ_α	Density during the respective flight state
σ_α	Nozzle exit ratio for hover flight